Elastic constants of single-crystal $TiN_x(001)$ $(0.67 \leqslant x \leqslant 1.0)$ determined as a function of x by picosecond ultrasonic measurements

Taeyoon Lee, K. Ohmori, C.-S. Shin, David G. Cahill, I. Petrov, and J. E. Greene
Department of Materials Science and the Fredrick Seitz Materials Research Laboratory, University of Illinois, 104 South Goodwin, Urbana, Illinois 61801, USA

(Received 11 November 2004; revised manuscript received 1 February 2005; published 13 April 2005)

The elastic constants c_{11} and c_{44} of single-crystal NaCl-structure δ-$TiN_x(001)$ layers, with x ranging from 0.67 to 1.0, were determined using sound velocity measurements. Picosecond ultrasonic optical pump/probe techniques were employed to generate and detect longitudinal sound waves and surface acoustic waves (SAW) in order to obtain $c_{11}(x)$ and $c_{44}(x)$, respectively. SAW generation was achieved by depositing a periodic series of Al bars on the $TiN_x(001)$ layers to spatially modulate the surface reflectivity. c_{11} and c_{44} were found to decrease continuously from 626 and 156 GPa with $x=1$ to 439 and 92 GPa with $x=0.67$. The Voit–Reuss–Hill average aggregate elastic moduli $E_{VRH}(x)$ obtained from our measured $c_{11}(x)$ and $c_{44}(x)$ values are in good agreement with previous $TiN_x(001)$ nanoindentation results.

DOI: 10.1103/PhysRevB.71.144106 PACS number(s): 62.20.Dc

I. INTRODUCTION

NaCl-structure δ-TiN_x thin films are widely used as hard wear-resistant coatings on cutting tools, as diffusion barriers in microelectronic devices, and as corrosion and abrasion resistant layers on optical components. In most of these applications, the δ-TiN_x coatings are deposited by reactive magnetron sputtering as substoichiometric layers in order to maximize the film growth rate by decreasing the N_2 fraction in mixed Ar/N_2 discharges.[1–3] Experimental investigations of polycrystalline δ-TiN_x, which has a wide single-phase field extending from $x \simeq 0.6$ to $\simeq 1.2$,[1] show that optical, electronic, and mechanical properties are a strong function of x due to changes in bonding, charge carrier density, and microstructure.[4]

The effect of N vacancies on the mechanical properties of substoichiometric TiN_x has been controversial. The hardness of polycrystalline TiN_x layers grown by reactive magnetron sputtering was reported to increase with decreasing x.[5] However, the opposite behavior has also been observed for both bulk[6] and sputter-deposited TiN_x.[1,7] The differences arise primarily from large variations in layer microstructures, which depend on growth and processing parameters, including average grain size, grain size distribution, texture, density, and strain state.

The hardness of a material depends on kinetic factors such as the nucleation rate and mobility of dislocations but for many transition metal nitrides and carbides, the experimentally observed hardness approaches the theoretical limit of $G/2\pi$, where G is the shear modulus. Therefore, an understanding of the dependence of the elastic constants on point defect concentration[8–10] or composition[11–13] is needed to fully understand the changes in hardness that accompany changes in vacancy concentrations or alloy composition. Elastic constants of disordered transition metal nitrides and carbides can be calculated from first principles;[8–12] to the best of our knowledge, however, these calculations have not been thoroughly validated by precise measurements of the elastic constants of well-characterized materials. In our previous work (Shin *et al.*[14]), we showed that the nanoindentation hardness H of well-characterized TiN_x single crystal layers grown on MgO(001) increases with increasing N-vacancy concentration ("vacancy hardening") with H ranging from 20 ± 2 GPa for $x=1.0$ to 30 ± 2 GPa for $x=0.67$. The elastic modulus E obtained from the nanoindentation measurements decreased from 430 ± 30 to 330 ± 20 GPa over the same range in x. However, since nanoindentation measurements are a complex average over crystal orientation, the fundamental elastic constants of $TiN_x(001)$ are still unknown.

To better understand the effects of N vacancies on the elastic properties of $TiN_x(001)$, we have determined the elastic constants c_{11} and c_{44} as a function of x from measurements of sound velocities using picosecond ultrasonic techniques. The approach, discussed by Tauc *et al.*,[15] has been widely used to generate and detect longitudinal sound waves in thin films and other nanostructures.[16,17] A subpicosecond pump light pulse focused onto a spot of diameter $\simeq 20$ μm on the surface of the sample, raises the local temperature a few degrees. This sets up a thermal stress which relaxes through the launching of an acoustic strain pulse that reflects from buried interfaces back to the surface where it alters the optical constants slightly and changes the optical reflectivity R by an amount ΔR. New reflectivities are measured by means of time-delayed probe light pulses applied at times t_i after the pump pulse. From these results, the longitudinal sound velocity of $TiN_x(001)$, which is directly related to the elastic constant $c_{11}(x)$, is determined.

Several surface acoustic wave (SAW) methods for determining the elastic constant c_{44} have been proposed recently. These techniques use a laser-generated SAW, the wavelength of which is determined by the interference of two beams intersecting the sample at different angles[18,19] and obtained by passing the incident beam through a diffraction mask[20] or an absorption grating etched into,[21] or deposited[22] onto, the sample. Time-delayed laser probe pulses are then used to obtain the SAW velocity. In the present experiments, we deposited separate sets of 45°-rotated patterned Al gratings on

$TiN_x(001)$ samples in order to measure the sound velocity along both the ⟨100⟩ and ⟨110⟩ directions, from which we obtain the elastic constant $c_{44}(x)$.

II. EXPERIMENTAL PROCEDURE

All $TiN_x(001)$ layers were epitaxially grown at 830 °C to a thickness of 260–340 nm on MgO(001) substrates in an ultrahigh vacuum dc magnetron sputter deposition system using the procedure described in Ref. 23. The target was a 7.6-cm-diameter 99.997% pure Ti disc and sputtering was carried out at a total pressure of 20 mTorr (2.67 Pa) in mixed discharges consisting of Ar (purity=99.9999%) and N_2(99.999%) with N_2 fractions f_{N_2} between 0.027 and 1.0. The film composition x varies nearly linearly from N/Ti =0.67 with $f_{N_2}=0.027$ to N/Ti=1.0 with $f_{N_2}=0.040$, thereafter remaining constant at $x=1$ as f_{N_2} is increased further to 1.0. The target current was 0.55 A, resulting in film growth rates ranging from 380 Å min^{-1} with f_{N_2} =0.027 to 86 Å min^{-1} with $f_{N_2}=1.0$.

$TiN_x(001)$ layer compositions x are determined by Rutherford backscattering spectrometry (RBS) and the spectra analyzed using the RUMP simulation program.[24] The uncertainty in reported N/Ti ratios is ±0.03. A combination of high-resolution x-ray diffraction (HR-XRD), plan-view transmission electron microscopy (TEM), and cross-sectional TEM (XTEM) were used to characterize film microstructure following the procedures described in Ref. 23. All $TiN_x(001)$ layers are NaCl structure with a cube-on-cube epitaxial relationship to the substrate, $(001)_{TiN}\|(001)_{MgO}$ and $[100]_{TiN}\|[100]_{MgO}$. Lattice parameters $a_\perp$ along the growth direction, in-plane lattice parameters $a_\|$, and residual strains ε were obtained from high-resolution reciprocal lattice maps (HR-RLMs) around asymmetric 113 reflections. The relaxed lattice constants $a_0(x)$ of TiN_x were found to decrease approximately linearly from 4.2397 Å with x =1.00 to 4.2333 Å with $x=0.92$ to 4.2305 Å with $x=0.82$, reaching 4.2256 Å at $x=0.67$, while the corresponding in-plane strain values in the films were −0.25%, −0.57%, −0.42%, and −0.37%, respectively.[23] While compressive strains generally increase the elastic constants of an epitaxial layer, the small strains in these films are not expected to alter them by more than a few percent.[25]

An Hitachi S4700 scanning electron microscope (SEM) with a field-emission source was used to measure the thicknesses h of cleaved cross-sectional $TiN_x(001)$ samples. Amorphous SiO_2 layers on Si(001), with thicknesses of 0.1 and 1 μm as verified by ellipsometry, served as calibration standards. Finite-thickness interference fringes, clearly visible in HR-XRD scans from all substoichiometric $TiN_x(001)$ layers, indicate that the films are of high structural quality with laterally uniform film/substrate interfaces. From the fringe spacing, we obtain layer thicknesses in good agreement with cross-sectional SEM results.

Mass densities ρ are obtained from a combination of RBS compositional measurements, atomic weights, and relaxed lattice constants $a_0(x)$ determined from HR-XRD scans by assuming that the deviation from stoichiometry is entirely due to N vacancies. The latter assumption is supported by *ab initio* density functional calculations.[14] Figure 1 is a plot of $TiN_x(001)$ mass density as a function of x. The mass density increases continuously from $\rho=5.078$ g/cm^3 with x =0.67 to $\rho=5.324$ g/cm^3 with $x=0.92$ to 5.399 g/cm^3 with $x=1.0$.

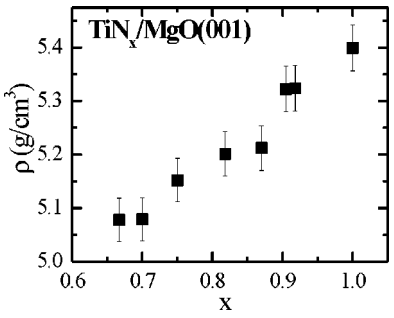

FIG. 1. Mass density ρ of epitaxial TiN_x layers grown on MgO(001) as a function of x.

We used a mode-locked Ti:sapphire laser operating at a wavelength $\lambda=770$ nm to generate the pump and probe pulses. For every composition x, we analyzed two different sets of $TiN_x(001)$ samples, one for determining longitudinal sound velocities and the other for SAW velocities. On the first set, used to measure sound velocities, 450-nm-thick Al blanket layers were deposited on $TiN_x(001)$ films to serve as transducers.

On the second $TiN_x(001)$ sample set, used to measure SAW velocities, we deposited 15 nm-thick Al layers, which were patterned by focused ion beam (FIB) etching to produce two absorption gratings, one with Al bars along ⟨100⟩ directions and the other with the bars along ⟨110⟩. The gratings consist of 150 parallel Al bars which are 220 nm wide and separated by 180 nm (i.e., the wavelength Λ is 400 nm). The absorbed pump-pulse energy launches an acoustic wave with the same spatial period as the grating in a direction orthogonal to the grating axis. This allows us to measure SAW velocities v_{SAW}^{100} and v_{SAW}^{110} along both major high-symmetry directions. Figure 2 shows a tapping-mode atomic force microscopy image of a small region of ⟨100⟩-oriented Al grating.

III. RESULTS AND DISCUSSION

Figure 3(a) is a typical plot of ΔR as a function of the time delay t between pump and probe pulses for a blanket Al-coated $TiN_x(001)$ sample, in this case with $x=1.0$. ΔR exhibits an initial rapid increase, due to local heating by the 0.3 ps pump laser pulse, followed by a slow decay. Superimposed on the intensity decay are small positive and negative peaks at times corresponding to acoustic pulses being reflected back to the surface from the buried Al/TiN_x (solid triangles and second open triangle) and TiN_x/MgO (first open triangle) interfaces. The positive (negative) change in ΔR results from a pulse which undergoes a phase shift by π (zero) due to reflection from an interface with a region of lower (higher) acoustic impedance Z.[26] This is illustrated schematically in Fig. 3(b). Since Z increases from air to Al to

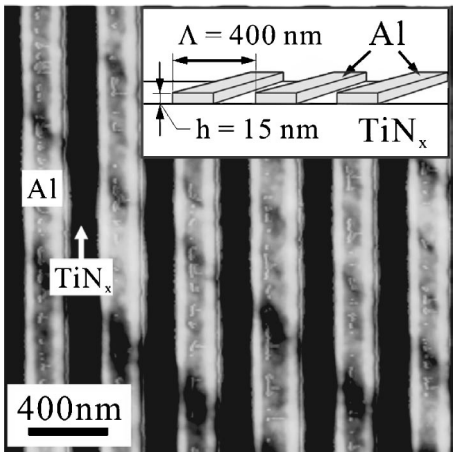

FIG. 2. AFM image of an Al grating formed on $TiN_x(001)$ layers. The grating consists of 150 parallel 15-nm-thick Al bars of width 220 nm and separated by 180 nm (the wavelength $\Lambda = 400$ nm). The inset is a schematic illustration of the sample geometry.

MgO to TiN_x, pulses reflected from the Al/TiN_x, TiN_x/MgO, and air/Al interfaces have phase shifts of zero, π, and zero, respectively. Hence, the signs of successive acoustic pulse echoes, corresponding to alternating positive and negative peaks, are determined by the interfacial boundary conditions.

The time interval t between any two adjacent peaks represented by solid and open symbols is constant and corresponds to the time t_{Al} required for the acoustic pulse to traverse the Al layer. Correspondingly, t_{TiN_x} is the time required for the pulse to travel through the $TiN_x(001)$ layer as defined in Fig. 3(a). The TiN_x longitudinal sound velocity v_l is then just given by $2h/t_{TiN_x}$, where h is the film thickness and $c_{11}=\rho v_l^2$ (Ref. 27) in which ρ is the layer density. Figure 4(a) is a plot of measured v_l values as a function of x. $v_l(x)$ decreases continuously from 10 770 m/s ($x=1.0$) to 9334 m/s ($x=0.67$), resulting in the elastic constant $c_{11}(x)$ decreasing from 626 GPa with $x=1$ to 439 GPa with $x=0.67$ as shown in Fig. 5(a).

Figure 3(c) is a plot of ΔR as a function of the time delay t for a SAW propagating perpendicular to the ⟨100⟩-oriented Al grating on a $TiN_x(001)$ sample with $x=0.67$. The amplitudes of SAW signals are quite small (of the order of 10^{-5}) compared to the initial increase in ΔR due to heating by the pump pulse. Thus, we offset the pump and probe beam positions by $\simeq 10$ μm perpendicular to the Al bars in order to isolate the SAW signal from the initial thermal response. The SAW velocity is $v_{SAW}=\Lambda/\tau_{SAW}$ where Λ is the wavelength of the Al grating and τ_{SAW} is the period of surface acoustic wave. For the results shown in Fig. 3(c), $\tau_{SAW}^{100}=93.35\pm0.84$ ps yielding $v_{SAW}^{100}=4285\pm38.9$ m/s for $TiN_{0.67}(001)$.

Measured v_{SAW}^{100} and v_{SAW}^{110} values for $TiN_x(001)$ are plotted in Fig. 4(b) as a function of x. v_{SAW}^{100} values are $\simeq 1\%$ higher than those of v_{SAW}^{110} at all $TiN_x(001)$ compositions. For stoichiometric TiN(001), as an example, $v_{SAW}^{100}=5125$ m/s and $v_{SAW}^{110}=5085$ m/s. Kim *et al.*[28] previously reported values of v_{SAW}^{100} and v_{SAW}^{110}, obtained using line-focus acoustic microscopy, as a function of the effective thickness, $\bar{h}=h/\Lambda$, of single-crystal stoichiometric TiN(001) layers. However, the films were rather thin, $0.01<\bar{h}<0.12$, and SAW velocities obtained from such thin layers vary with film

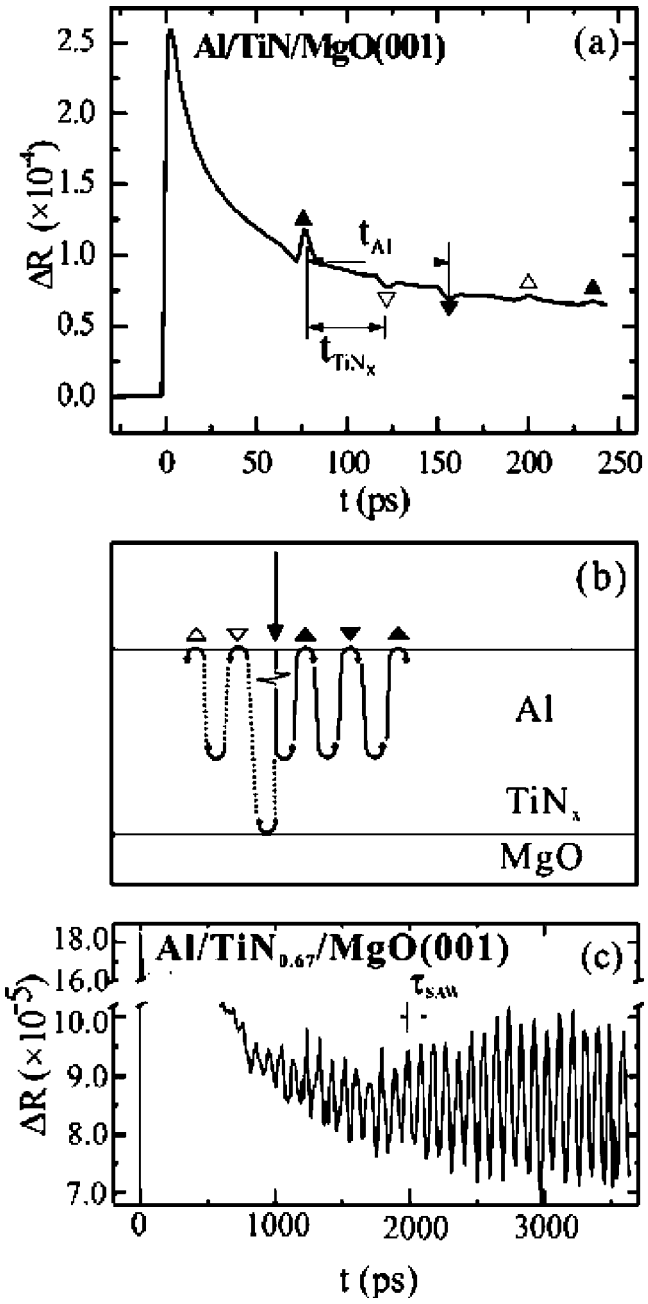

FIG. 3. (a) A typical plot of the change in reflectivity ΔR as a function of the time delay t between laser pump and probe pulses incident on a blanket-Al-coated stoichiometric TiN(001) sample. The solid triangles indicate ΔR peaks corresponding to acoustic pulses reflected from the Al/TiN_x interface. The open triangles mark ΔR peaks corresponding to additional reflections from TiN_x/MgO (▽) and Al/TiN_x (△) interfaces as shown schematically in (b). (c) A plot of ΔR as a function of the time delay t for a SAW propagating perpendicular to a ⟨100⟩-oriented Al grating on $TiN_{0.67}(001)$.

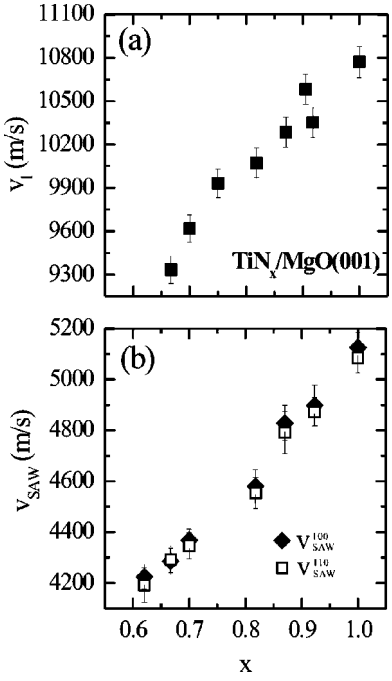

FIG. 4. (a) Measured longitudinal sound velocity v_1 and (b) surface acoustic wave (SAW) velocities v^{100}_{SAW} and v^{110}_{SAW} along ⟨100⟩ and ⟨110⟩ directions in epitaxial TiN$_x$(001) as a function of x.

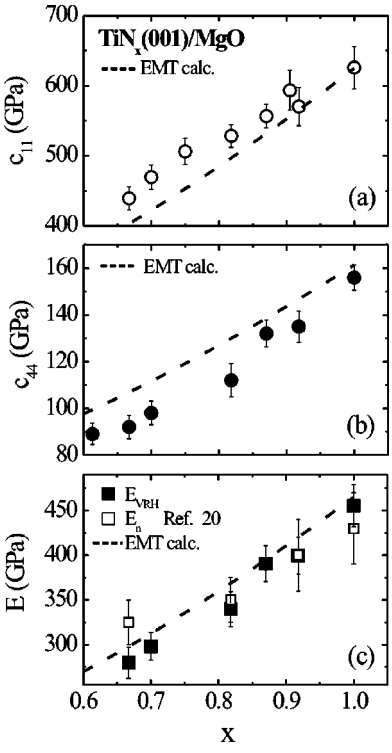

FIG. 5. TiN$_x$(001) elastic constants (a) c_{11} and (b) c_{44} plotted as a function of x. (c) The Voigt–Reuss–Hill elastic moduli E_{VRH}, calculated from our $c_{11}(x)$ and $c_{44}(x)$ results, and nanoindentation (E_n) elastic moduli (Ref. 20) vs x. The dashed lines in all three panels were calculated using Bruggeman effective medium theory (EMT).

thickness since the surface wave penetrates significantly into the substrate. In the present experiments, we used much shorter SAW wavelengths Λ. Thus, the effective thickness of our TiN$_x$(001) layers is $0.60 < \overline{h} < 1.0$ for which there is no significant substrate effect (i.e., v_{SAW} is essentially independent of $\overline{h}$).

To obtain $c_{44}(x)$ values, we use the matrix approach (MA), a numerical method developed by Fahmy and Alder[29] for describing layered materials systems. Each layer is characterized by means of a transfer matrix which contains information concerning mechanical properties of the layer, including material stiffnesses at the boundary planes.[30,31] In its usual form, the MA approach is used to obtain SAW propagation velocities from known elastic constants (c_{11}, c_{12}, and c_{44}) and the density ρ of each layer in the multilayer. In the present case, we start with our measured $v_{\mathrm{SAW}}(x)$ values and obtain the elastic constants of TiN$_x$(001) in a two-layer system, TiN$_x$/MgO(001).

The calculated TiN$_x$(001) SAW propagation velocity v_{calc}, obtained by the MA method, is a function of eight parameters, the densities of TiN$_x$(ρ_{TiN_x}) and MgO [$\rho_{\mathrm{MgO}} = 3.598$ g/cm^3 (Ref. 28)], the three TiN$_x$ elastic constants (c_{11}, c_{12}, and c_{44}), and the elastic constants of MgO [$c_{11} = 299.8$ GPa, $c_{12} = 99.1$ GPa, and $c_{44} = 157.5$ GPa (Ref. 28)]. Since $\rho_{\mathrm{TiN}_x}(x)$ (see Fig. 1) and $c_{11}(x)$ [Fig. 5(a)] are known for TiN$_x$(001), there are only two degrees of freedom for v_{calc}, the c_{12} and c_{44} elastic constants for TiN$_x$. These two degrees of freedom are linked by the elastic anisotropy factor η (Ref. 32),

$$\eta = 2c_{44}/(c_{11} - c_{12}). \tag{1}$$

The anisotropy factors $\eta(x)$ for TiN$_x$(001) ($0.67 \leqslant x < 1.0$) are unknown. However, v_{SAW} is insensitive to c_{12}; $(c_{12}/v_{\mathrm{SAW}})(\partial v_{\mathrm{SAW}}/\partial c_{12}) \simeq 0.025$, while $(c_{44}/v_{\mathrm{SAW}})(\partial v_{\mathrm{SAW}}/\partial c_{44}) \simeq 0.5$. Thus, we assume that η for substoichiometric TiN$_x$(001) is equal to that of stoichiometric TiN(001) [$\eta_{\mathrm{TiN}} = 0.71$ (Ref. 28)]. This reduces the SAW propagation velocity calculated by the MA method to a function of a single parameter, $v_{\mathrm{calc}}(c_{44})$. For each TiN$_x$(001) composition, we begin by estimating c_{44} and computing v_{calc}. Then, we compare the $v_{\mathrm{calc}}(x)$ values to our measured $v_{\mathrm{SAW}}(x)$ values, input new estimates for $c_{44}(x)$, and continue this iterative procedure until we obtain the best agreement between the calculated and measured SAW propagation velocities. Figure 5(b) is a plot of the resulting c_{44} values as a function of x. c_{44} decreases continuously from 156 GPa with $x = 1$ to 92 GPa with $x = 0.67$.

In order to compare our measurements of the elastic constants $c_{11}(x)$ and $c_{44}(x)$ with the elastic moduli (Young's moduli) E_n (Ref. 14) obtained from previous TiN$_x$(001) nanoindentation measurements, which are average over many orientations, we use the Voigt–Reuss–Hill (VRH) method[33,34] to first calculate isotropic moduli E_{VRH} as a function of $c_{11}(x)$ and $c_{44}(x)$. Assuming uniform local strain, Voigt derived expressions for the isotropic bulk modulus K_V and shear modulus G_V of a polycrystalline material based

upon the three principal elastic constants of a cubic single crystal,[35]

$$K_V = (c_{11} + 2c_{12})/3, \tag{2a}$$

$$G_V = (c_{11} - c_{12} + 3c_{44})/5. \tag{2b}$$

Reuss developed corresponding expressions for K_R and G_R assuming uniform local stress instead of uniform strain,[35]

$$1/K_R = 3s_{11} + 6s_{12}, \tag{3a}$$

$$15/G_R = 12s_{11} - 12s_{12} + 9s_{44}, \tag{3b}$$

where s_{ij} are elastic compliances. Subsequently, Hill[33,34] proved that the actual moduli are bounded by the expressions due to Voigt and Reuss, i.e., K_V, $G_V > K$, $G > K_R$, G_R. The average of these limiting values provides practical estimates for the moduli of isotropic materials,

$$K_H = 1/2(K_R + K_V), \tag{4a}$$

$$G_H = 1/2(G_R + G_V). \tag{4b}$$

The elastic modulus E_{VRH}, given by what is now termed the Voigt–Reuss–Hill method,[33], is

$$E_{\mathrm{VRH}} = \frac{9K_H G_H}{3K_H + G_H}. \tag{5}$$

For elastic constants comparable to TiN, the elastic modulus E_{VRH} is only weakly dependent on c_{12}; for example, an error of 20% in our estimate of c_{12} will propagate into only a 1.4% error in E_{VRH}. Figure 5(c) is a plot of both E_{VRH} (solid symbols) and E_n (Ref. 14) (open symbols) as a function of x. E_{VRH} values decrease continuously with x from $E_{\mathrm{VRH}} \simeq 455$ GPa for stoichiometric TiN(001) ($x=1.0$) to $E_{\mathrm{VRH}} \simeq 280$ GPa for $x=0.67$ and the results in Fig. 5(c) show that $E_{\mathrm{VRH}}(x)$ and $E_n(x)$ values are in remarkably good agreement. We attribute the small discrepancy ($\lesssim 10\%$) to complex nonhomogeneous stress fields produced by the indentor tip which do not average E equally over all directions in the sample, but gives more weight to the loading direction (001) which corresponds to the lowest E of the low-index orientations.[36]

To gain further insight into the effects of the N-vacancy concentration on the elastic properties of $TiN_x(001)$, we employ Bruggeman″s effective medium theory (EMT)[37] which provides estimates of the effective elasticity of composite materials. Here, we treat substoichiometric $TiN_x(001)$ as an isotropic mixtures of $(TiN)_x$ and Ti_{1-x}. In the coherent potential approximation (CPA)[37] for a two-component material, an effective elastic property K^* (where K represents c_{11}, c_{44}, or E) is expressed as a function of the corresponding values $K^{(1)}$ and $K^{(2)}$ of the component materials,

$$K^*(x) = \theta(x) + [\theta^2(x) + K^{(1)}K^{(2)}]^{1/2}, \tag{6a}$$

where

$$\theta(x) = \tfrac{1}{2}(K^{(1)} - K^{(2)})(1 - 2x). \tag{6b}$$

Using previously reported values of the elastic constants and modulus of stoichiometric TiN ($c_{11}=625$ GPa, $c_{44}=163$ GPa, and $E_{\mathrm{VRH}}=465$ GPa,[28] which are in good agreement with the present results) and fcc Ti [$c_{11}=136$ GPa, $c_{12}=92$ GPa, and $c_{44}=61$ GPa, and $E_{\mathrm{VRH}}=113.9$ GPa (Ref. 38)], we calculate effective $c_{11}{}^*(x)$, $c_{44}{}^*(x)$, and $E_{\mathrm{VRH}}{}^*(x)$ values and plot them as dashed lines in Figs. 5(a)–5(c). The agreement between $c_{11}{}^*(x)$, $c_{44}{}^*(x)$, and $E_{\mathrm{VRH}}{}^*(x)$ and our measured values $c_{11}(x)$, $c_{44}(x)$, and $E_{\mathrm{VRH}}(x)$ is quite good given the fact that EMT assumes elastic isotropy while $TiN_x(001)$ is anisotropic.

IV. CONCLUSIONS

The longitudinal sound velocity v_l, the surface acoustic wave velocities v_{SAW}^{100} and v_{SAW}^{110}, and the elastic constants c_{11} and c_{44} of single crystal $TiN_x(001)$ ($0.67 \leqslant x \leqslant 1.0$) layers have been determined as a function of the N/Ti ratio x using picosecond ultrasonic pump/probe measurements. v_l, v_{SAW}^{100}, and v_{SAW}^{110} all decrease continuously with increasing N vacancy concentration, ranging from 10771, 5125, and 5085 m/s for stoichiometric TiN(001) to 9334, 4285, and 4293 m/s for substoichiometric $x=0.67$ layers. Corresponding values for $c_{11}(x)$ and $c_{44}(x)$ decrease from 626 and 156 GPa with $x=1$ to 439 and 92 GPa with $x=0.67$. Orientation-averaged elastic moduli $E_{\mathrm{VRH}}(x)$, obtained using our measured $c_{11}(x)$ and $c_{44}(x)$ results in conjunction with the Voigt–Reuss–Hill model, exhibit good agreement with previously published $TiN_x(001)$ nanoindentation results[14] carried out as a function of x.

ACKNOWLEDGMENTS

This research was supported by the U.S. Department of Energy, Division of Materials Science, Grant No. DEFG02-91ER45439 through the University of Illinois Frederick Seitz Materials Research Laboratory. The authors deeply appreciate fruitful discussions with J. Bareno, S. Kodambaka, and H. Hwang. We also appreciate the use of the facilities of the FS-MRL Center for Microanalysis of Materials, which is partially supported by DOE, at the University of Illinois.

[1] J.-E. Sundgren, B.-O. Johansson, A. Rockett, S. A. Barnett, and J. E. Greene, in *Physics and Chemistry of Protective Coatings*, edited by J. E. Greene, W. D. Sproul, and J. A. Thornton (American Institute of Physics, New York, 1986), Ser. 149, p. 95.

[2] W. D. Sproul, Thin Solid Films **107**, 141 (1984).

[3] I. Petrov, A. Myers, J. E. Greene, and J. R. Abelson, J. Vac. Sci. Technol. A **12**, 2846 (1994).

[4] P. E. Schmid, M. S. Sunage, and F. Levy, J. Vac. Sci. Technol. A **16**, 2870 (1998); J. H. Kang and K. J. Kim, J. Appl. Phys. **86**,

346 (1999); P. Patsalas and S. Logothetidis, *ibid.* **90**, 4725 (2001).
[5] J. Chevallier, J. P. Chabert, and J. Spitz, Thin Solid Films **80**, 263 (1981); M. K. Hibbs, B. O. Johansson, J.-E. Sundgren, and U. Helmersson, *ibid.* **122**, 115 (1984); J. Musil, S. Kadlec, J. Vyskočil, and V. Valvoda, *ibid.* **167**, 107 (1988).
[6] J.-E. Sundgren and H. T. G. Hentzell, J. Vac. Sci. Technol. A **4**, 2259 (1986), and references therein.
[7] X. Jiang, M. Wang, K. Schmidt, E. Dunlop, J. Haupt, and W. Gissler, J. Appl. Phys. **69**, 3053 (1991); J. Kohlscheen, H. R. Stock, and P. Mayr, Surf. Coat. Technol. **120–121**, 740 (1999); H. Holleck, J. Vac. Sci. Technol. A **4**, 2661 (1986).
[8] S.-H. Jhi, S. G. Louie, M. L. Cohen, and J. Ihm, Phys. Rev. Lett. **86**, 3348 (2001).
[9] M. Guemmaz, A. Mosser, R. Ahujab, and B. Johansson, Solid State Commun. **110**, 299 (1999).
[10] Z. Dridi, B. Bouhafs, P. Ruterana, and H. Aourag, J. Phys.: Condens. Matter **14**, 10237 (2002).
[11] S.-H. Jhi, J. Ihm, S. G. Louie, and M. L. Cohen, Nature (London) **399**, 132 (1999).
[12] K. Chen, L. R. Zhao, J. Rodgers, and J. S. Tse, J. Phys. D **36**, 2725 (2003).
[13] Q. Yang, W. Lengauer, T. Koch, M. Scheere, and I. Smid, J. Alloys Compd. **309**, L5 (2000).
[14] C.-S. Shin, D. Gall, N. Hellgren, J. Patscheider, I. Petrov, and J. E. Greene, J. Appl. Phys. **93**, 6025 (2003).
[15] C. Thomsen, H. T. Grahn, H. J. Maris, and J. Tauc, Phys. Rev. B **34**, 4129 (1986).
[16] G. A. Antonelli, H. J. Maris, S. G. Malhotra, and J. M. E. Harper, J. Appl. Phys. **91**, 3261 (2002).
[17] K. E. O'Hara, X. Hu, and D. G. Cahill, J. Appl. Phys. **90**, 4852 (2001).
[18] Q. Shen, A. Harata, and T. Sawada, Jpn. J. Appl. Phys., Part 1 **35**, 2339 (1996).
[19] T. F. Crimmins, A. A. Maznev, and K. A. Nelson, Appl. Phys. Lett. **74**, 1344 (1999).
[20] G. A. Antonelli, P. Zannitto, and H. J. Maris, Physica B **316**, 377 (2002).
[21] L. Dhar and J. A. Rogers, Appl. Phys. Lett. **77**, 1402 (2000).
[22] D. H. Hurley and K. L. Telschow, Phys. Rev. B **66**, 153301 (2002).
[23] C.-S. Shin, S. Rudenja, D. Gall, N. Hellgren, T.-Y. Lee, I. Petrov, and J. E. Greene, J. Appl. Phys. **95**, 1 (2004).
[24] R. L. Doolittle, Nucl. Instrum. Methods Phys. Res. B **15**, 344 (1985).
[25] J. A. Floro, E. Chason, S. R. Lee, and G. A. Petersen, Appl. Phys. Lett. **71**, 1694 (1997).
[26] The acoustic impedance of a material is given by $Z=\rho v$, where ρ is the mass density and v is the sound velocity. ρ and v values for Al and MgO were taken from J. W. Swegle and D. E. Grady, J. Appl. Phys. **58**, 692 (1985).
[27] G. W. Farnell, in *Physical Acoustics*, edited by W. P. Mason and R. N. Thurston (Academic, New York, 1970), Vol. 4, Chap. 3.
[28] J. O. Kim, J. D. Achenbach, P. B. Mirkarimi, M. Shinn, and S. A. Barnett, J. Appl. Phys. **72**, 1805 (1992).
[29] A. H. Fahmy and E. L. Alder, Appl. Phys. Lett. **22**, 495 (1973).
[30] E. L. Adler, IEEE Trans. Ultrason. Ferroelectr. Freq. Control **37**, 485 (1990).
[31] E. L. Adler, J. K. Slaboszewicz, G. W. Farnell, and C. K. Jen, IEEE Trans. Ultrason. Ferroelectr. Freq. Control **37**, 215 (1990).
[32] D. C. Gazis, R. Herman, and R. F. Wallis, Phys. Rev. **119**, 533 (1960).
[33] O. L. Anderson, J. Phys. Chem. Solids **63**, 909 (1963).
[34] R. Hill, Proc. Phys. Soc. London **65**, 350 (1952).
[35] H. B. Huntington, in *Solid State Phyics: Advanced in Research and Applications*, edited by F. Seitz and D. Turnbull (Academic, New York, 1958), Vol. 7, Chap. 3, p. 222.
[36] H. Ljungcrantz, M. Oden, L. Hultman, J. E. Greene, and J.-E. Sundgren, J. Appl. Phys. **80**, 6725 (1996).
[37] J. G. Berryman, J. Acoust. Soc. Am. **91**, 551 (1992).
[38] We use c_{ij} and E values reported in A. Aguayo, G. Murrieta, and R. de Coss, Phys. Rev. B **65**, 092106 (2002); S. K. Kim, F. Jona, and P. M. Marcus, J. Phys.: Condens. Matter **8**, 25 (1996); P. M. Marcus and F. Jona, *ibid.* **9**, 6241 (1997) for face-centered-cubic Ti ($c_{11}=136$ GPa, $c_{12}=92$ GPa, $c_{44}=61$ GPa, and $E_{\mathrm{VRH}}=113.9$ GPa).